

UC Santa Barbara

UC Santa Barbara Previously Published Works

Title

Enhancing Thermoelectric Properties through Control of Nickel Interstitials and Phase Separation in Heusler/Half-Heusler TiNi_{1.1}Sn Composites

Permalink

<https://escholarship.org/uc/item/0ks7r611>

Journal

Materials, 11(6)

ISSN

1996-1944

Authors

Levin, Emily
Long, Francesca
Douglas, Jason
et al.

Publication Date



2018-05-28

DOI

10.3390/ma11060903

Peer reviewed

Enhancing Thermoelectric Properties through Control of Nickel Interstitials and Phase Separation in Heusler/Half-Heusler $\text{TiNi}_{1.1}\text{Sn}$ Composites

Emily E. Levin^{1,2} , Francesca Long,^{1,2,†} Jason E. Douglas,^{1,2,‡} Malinda L. C. Buffon,^{1,2,§} Leo K. Lamontagne,^{1,2} Tresa M. Pollock,^{1,2} and Ram Seshadri^{1,2,*} 

¹ Materials Department, University of California, Santa Barbara, CA 93106

² Materials Research Laboratory, University of California, Santa Barbara, CA 93106

* Correspondence: Ramseshadri@ucsb.edu; Tel.: +1-805-893-6129

† Current address: Department of Materials Science and Engineering, Northwestern University, Evanston, IL 60208

‡ Current address: Materials Science and Engineering Division, NIST, Gaithersburg, MD 20899

§ Current address: Intel Corporation, Hillsboro, OR 97124

Abstract: Thermoelectric devices, which allow direct conversion of heat into electrical energy, require materials with improved figures of merit (zT) in order to ensure widespread adoption. Several techniques have been proposed to increase the zT of known thermoelectric materials through reduction of thermal conductivity, including heavy atom substitution, grain size reduction, and inclusion of a semicoherent second phase. The goal in these approaches is to reduce thermal conductivity through phonon scattering without modifying electronic properties. In this work we demonstrate that Ni interstitials in the half-Heusler thermoelectric TiNiSn can be created and controlled in order to improve physical properties. Ni interstitials in $\text{TiNi}_{1.1}\text{Sn}$ are not thermodynamically stable, and instead are kinetically trapped using appropriate heat treatments. The Ni interstitials, which act as point defect phonon scattering centers and modify the electronic states near the Fermi level, result in reduced thermal conductivity and enhance the Seebeck coefficient. The best materials tested here, created from controlled heat treatments of $\text{TiNi}_{1.1}\text{Sn}$ samples, display $zT = 0.26$ at 300 K; the largest value reported for compounds in the Ti–Ni–Sn family.

Keywords: Heusler; TiNiSn ; TiNi_2Sn ; Point defect; Thermoelectric; Phonon scattering

1. Introduction

Thermoelectric materials, which convert between thermal and electric energy through solid state phenomena, have the potential to harvest waste heat, therefore reducing energy consumption and greenhouse gas production.[1] While thermoelectrics currently have a variety of niche uses such as thermoelectric radioisotope generators in space probes, the widespread adoption of thermoelectric technology awaits more efficient devices, whose efficiency depends on the figure of merit (zT) of the materials employed.[2,3] The figure of merit is given by the equation $zT = [S^2 / (\rho \kappa)]T$ where S , ρ , κ , and T are the Seebeck coefficient, electrical resistivity, thermal conductivity, and temperature, respectively. These properties are interrelated, frequently making it difficult to improve overall zT . [1,4] For example, increasing the electrical conductivity (decreasing ρ) will increase thermal conductivity due to the electronic contribution to κ . However, the lattice contribution to κ can be reduced independently by the insertion of phonon scattering centers.[3,5,6] Engineering advanced materials through techniques to enhance phonon scattering across different length scales such as doping and heavy atom substitution,[7–11] micro/nanostructuring through grain size reduction,[3,10,12,13] and

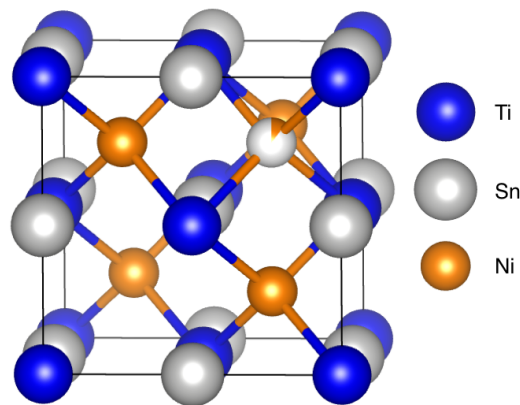


Figure 1. Crystal structure of half-Heusler TiNiSn in the $F\bar{4}3m$ space group. Excess Ni occupies vacant tetrahedral sites, as shown by the partially occupied Ni interstitial. All four of the vacant tetrahedral sites are filled in the full Heusler, in the space group $Fm\bar{3}m$.

29 phase separation[14–22] have been shown to increase the figure of merit of known thermoelectric
 30 materials. State-of-the-art thermoelectric materials such as Bi_2Te_3 and AgSbTe_2 exhibit values of $zT \approx 1$
 31 to 1.5 at their optimal operation temperature.[1,23–26]

32 Half-Heusler materials are promising for middle-to-high temperature range (600 K to 900 K)
 33 thermoelectric applications due to their intrinsically high power factor (S^2/σ), despite their high
 34 thermal conductivity. Douglas *et al.* have shown that hierarchal microstructural engineering through
 35 the inclusion of a semicoherent second phase in TiNiSn decreases thermal conductivity by scattering
 36 phonons at multiple length scales.[3,10,15,27] In this compound, the addition of excess Ni leads to
 37 phase separation between the full and half-Heusler upon solidification. The two phases are immiscible
 38 at moderate temperatures. However, the phase diagram presented by Verma *et al.* suggests both regions
 39 of phase separation and phase solubility can be accessed at the composition $\text{TiNi}_{1.1}\text{Sn}$. [28] At high
 40 temperatures, the excess Ni fills the tetrahedral voids in the half-Heusler crystal structure, shown in
 41 Figure 1.[27,29,30] Hazama *et al.* has shown that $\text{TiNi}_{1+x}\text{Sn}$ follows Vegard’s law, with the lattice
 42 parameter expanding linearly with the addition of nickel.[31,32] In this work, heat treatments are
 43 used to trap these Ni interstitials, and properties are analyzed as a function of the prevalence of Ni
 44 interstitials and microstructure.

45 Nickel interstitials act as point defect scattering centers for phonons, reducing the thermal
 46 conductivity through alloys scattering.[32–34] In addition, these interstitials modify the electronic
 47 structure near the Fermi energy, providing “in-gap states” which affect the Seebeck coefficient and
 48 electrical resistivity.[35,36] Miyamoto *et al.* observed these “in-gap states” using X-ray photoemission
 49 spectroscopy on stoichiometric TiNiSn, and attributed these states to the atomic disorder present
 50 when Ni sits on the vacant site. The variability in reported zT of the half-Heusler TiNiSn is likely
 51 due to the presence of varying amounts of Ni interstitials, which is highly dependent on processing
 52 conditions.[30,33,35] In this contribution, the disorder is built in by using heat treatments to modify
 53 the occupancy of Ni on the vacant site rather than the use of additional alloying elements. As shown
 54 here, the processing conditions and thermal history of TiNiSn compounds are extremely important to
 55 the prevalence of Ni-interstitials and microstructure, which have large effects on the physical properties.
 56 By contributing these insights on the relationship between processing, structure, and thermoelectric
 57 performance of TiNiSn, this work enables both the understanding of fundamental concepts behind
 58 defect-engineering and the development of high performance thermoelectric materials.

59 2. Experimental details

60 Four $\text{TiNi}_{1.1}\text{Sn}$ samples were melted utilizing a Crystalox MCGS5 levitation melting system with
 61 a water cooled copper crucible under an Ar atmosphere. Charges of approximately 12 g were formed

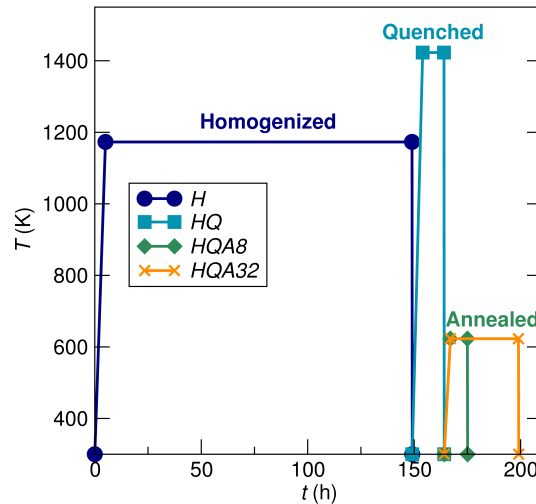


Figure 2. Nature of heat treatments employed in this study. Four samples were prepared: *H*, *HQ*, *HQA8*, and *HQA32*. With the exception of the final anneals for *HQA8* and *HQA32*, heat treatments were applied to samples simultaneously.

62 from a stoichiometric ratio of $\text{TiNi}_{1.1}\text{Sn}$ from elemental sources: Ti wire (99.7%, Sigma Aldrich),
 63 Ni foil (99.9%, Sigma Aldrich), and Sn shot (99.8%, Sigma Aldrich). As visualized in Figure 2,
 64 heat treatments were applied to each sample. The *Homogenized (H)* sample was held at 1173 K for
 65 144 h (6 d), after which the sample was air-quenched. The *Homogenized-Quenched (HQ)* sample was
 66 homogenized with *H* and was subsequently brought to 1423 K for 6 h from which it was air-quenched.
 67 The *Homogenized-Quenched-Annealed-8 h (HQA8)* sample followed the same heat treatment as *H* and
 68 *HQ*, and was then annealed for 8 h at 623 K. Similarly, *Homogenized-Quenched-Annealed-32 h (HQA32)*
 69 was heat-treated with the other samples, but annealed for 32 h at 623 K. All heat treatments were
 70 conducted by wrapping the samples in Ta foil and sealing in a fused silica ampoule under vacuum.
 71 Samples were sectioned by diamond saw for experiments, including a piece to grind into powder for
 72 synchrotron X-ray diffraction, a piece for scanning electron microscopy, and a bar for physical property
 73 measurements, approximately $8 \times 3 \times 3$ mm.

74 Synchrotron X-ray diffraction (XRD) data was acquired at the 11-BM beamline at the Advanced
 75 Photon Source at Argonne National Lab. Measurements were conducted at 295 K and run at a modified
 76 wavelength ($\lambda = 0.460461 \text{ \AA}$) to reduce Sn absorbance. Rietveld refinement analysis was completed on
 77 diffraction data using TOPAS.[37] Crystal structures were visualized using VESTA.[38]

78 Samples of *H*, *HQ*, and *HQA32* were prepared for microstructure evaluation using scanning
 79 electron microscopy by mounting a piece from the bulk samples in epoxy, and polishing with diamond
 80 suspension down to $0.25 \mu\text{m}$. Studies were conducted on a FEI XL30 Sirion FEG scanning electron
 81 microscope (SEM) equipped with a backscattered-electron (BSE) detector and energy dispersive X-ray
 82 (EDS) spectrometer, enabling phase observation and composition determination. Values for composition
 83 are averaged over several EDS point measurements. Electron transparent lamellae were prepared using
 84 a focused ion beam (FIB, Helios, FEI) and characterized using a FEI Tecnai G2 Sphera transmission
 85 electron microscope (TEM).

86 Electrical transport properties (Seebeck coefficient and electrical resistivity) were evaluated on
 87 an ULVAC ZEM-3 instrument under a partial He atmosphere. Measurements were conducted at
 88 310 K. Thermal conductivity measurements were conducted on a Quantum Design Physical Property
 89 Measurement System (PPMS) utilizing the Thermal Transport Option (TTO). At elevated temperatures,
 90 Ni interstitials that have been trapped in the half-Heusler structure are able to diffuse, changing the
 91 nickel distribution. Due to the effect of high temperature measurements on samples, measurements
 92 were taken between 300 K and 310 K.[28]

Table 1. Heat treatments for each sample are given. Values for goodness of fit (R_{wp}), mole percent of the full Heusler phase, and the weighted average lattice parameter of the half-Heusler phases (hH a_{av}) with Ni interstitials are determined from the Rietveld refinement of synchrotron XRD data.

Sample	Treatment	R_{wp} (%)	fH mol%	hH a_{av} (Å)
<i>H</i>	1173 K 144 h	9.75	12.7	5.918(2)
<i>HQ</i>	1173 K 144 h	12.0	8.6	5.969(1)
	1423 K 6 h + <i>Q</i>			
<i>HQA8</i>	1173 K 144 h	13.1	7.8	5.948(3)
	1423 K 6 h + <i>Q</i>			
	623 K 8 h			
<i>HQA32</i>	1173 K 144 h	15.4	8.8	5.947(2)
	1423 K 6 h + <i>Q</i>			
	623 K 32 h			

93

94 3. Results and discussion

95 *Structural characterization*

96 The high signal-to-noise ratio of synchrotron X-ray diffraction (SXR) enables precise analysis of
 97 half-Heusler and Heusler phase fractions using Rietveld refinement, as well as identification of secondary
 98 phases. Small amounts ($< 3\%$) of Sn and Sn_5Ti_6 were identified. The fine Q -space resolution of this
 99 technique allows for the evaluation of accurate lattice parameters, and the observation of the asymmetry
 100 in peaks corresponding to different lattice parameters in the half-Heusler phase due to changing Ni
 101 content. Refinements of SXR are shown in Figure 3, including individual phase contributions from
 102 major phases.

103 The half-Heusler TiNiSn , in the space group $F\bar{4}3m$, consists of four interpenetrating fcc sublattices,
 104 one of which is vacant (Figure 1). The covalent nature of the $[\text{NiSn}]$ sublattice is emphasized by viewing
 105 this as a zinc blende sublattice, with Ti occupying octahedral voids.[39] This structure containing 18
 106 valence electrons is valence precise, with 4 valence electrons per atom in the $[\text{NiSn}]^{4-}$ zinc blende
 107 network, making this compound semiconducting.[40] Excess Ni incorporated into the structure *via* heat
 108 treatments occupies the vacant tetrahedral sites, or the unoccupied sublattice.[29] A peak shift toward
 109 lower Q corresponds with a larger lattice parameter, implying a higher occupancy of Ni interstitials.

110 The enhanced view of the half-Heusler (220) peak in Figure 3 illustrates that multiple $\text{TiNi}_{1+x}\text{Sn}$
 111 phases with lattice parameters varying $\leq 0.4\%$ are necessary to fit the asymmetric peak shape.[27]
 112 This peak corresponds only to the half-Heusler, with no contributions from other phases. Fitting
 113 this asymmetry with multiple half-Heusler phases with different lattice parameters indicates an
 114 inhomogeneous distribution of Ni interstitials, rather than distinct half-Heusler phases. The occupancy of
 115 the second nickel site could not be fit due to the peak overlap, however a larger lattice parameter implies
 116 a higher nickel content. The asymmetry is present even in the homogenized (*H*) sample, meaning
 117 there are Ni interstitials present even in what should be pure TiNiSn . This is observed in stoichiometric
 118 TiNiSn , and likely leads to a wide spread of properties measured on different samples.[27] The weighted
 119 average lattice parameter of the half-Heusler phases (hH a_{av}) in each sample (see Table 1) gives an
 120 indication of the overall amount of Ni interstitials trapped in the half-Heusler structure. This can be
 121 qualitatively seen by the peak shifting in Q space, and is given in Figure 4. The homogenized sample
 122 (*H*) has phase separated, and the lattice parameter of the half-Heusler phase is low. For the composition
 123 $\text{TiNi}_{1.1}\text{Sn}$ at equilibrium, 10 mol% of the full Heusler phase is expected, but the homogenized sample
 124 has a larger than nominal percentage of the full Heusler phase. After treatment at high temperature and
 125 quenching (*HQ*), Ni interstitials are trapped and the average lattice parameter is maximized. In this
 126 sample, there is no half-Heusler without Ni interstitials. This treatment is accompanied by a decrease in

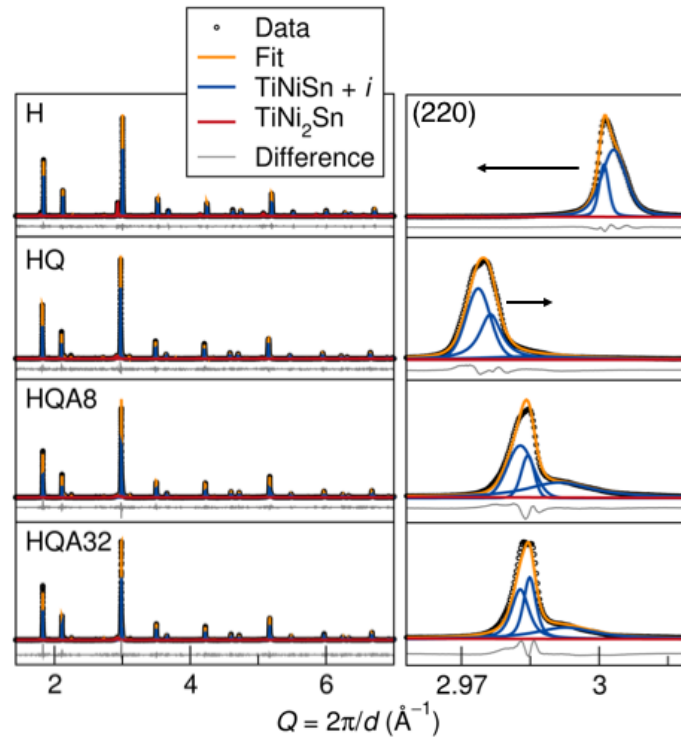


Figure 3. Rietveld refinement of synchrotron X-ray diffraction data for each sample, showing the individual contributions from each major phase present. The enhanced view of the (220) peak (right panel) shows asymmetry that must be fit using multiple phases with Ni-interstitials. The shifting of these peaks implies a larger lattice parameter of the $\text{TiNiSn} + i$ phase in the *HQ* sample, consistent with the theory that there are more kinetically trapped Ni interstitials due to the heat treatment.

127 the fraction of full Heusler, given in Table 1. The low temperature anneal (*HQA8* and *HQA32*) drives
 128 the system back towards equilibrium, and the lattice parameter decreases as Ni interstitials diffuse
 129 out of the half-Heusler. The tails on the peaks in the annealed samples are much more pronounced,
 130 signifying a wider Ni distribution. The full Heusler peak is also very broad in these samples, perhaps
 131 due to inhomogeneity or strain from the half-Heusler matrix.

132 *Microscopy*

133 The series of micrographs shown in Figure 5 were collected by SEM using a back-scattered electron
 134 (BSE) detector in order to evaluate the evolution of microstructure with heat treatment. BSE images
 135 show Z-contrast, allowing us to visually distinguish between phases, and to a lesser extent orientation
 136 contrast due to electron channeling.[41] Local EDS measurements elucidate the chemical composition
 137 of each phase. The homogenized sample, shown in Figure 5(a), shows phase separation between the full
 138 and half-Heusler phases, with the compositions $\text{Ti}_{0.98(1)}\text{Ni}_{1.78(2)}\text{Sn}_{1.00(1)}$ and $\text{Ti}_{0.97(1)}\text{Ni}_{1.03(1)}\text{Sn}_{1.00(1)}$,
 139 respectively. The TEM micrograph in Figure 6(a) confirms the micron-scale phase separation of the full
 140 and half-Heusler after the homogenization treatment. The semicoherent interface between half-Heusler
 141 precipitates and the Heusler phase shows evidence of misfit dislocations.[28] The 3% lattice mismatch
 142 between the full and half-Heusler phases produces strain fields extending in to each phase, which
 143 contribute to phonon scattering.[27] After the high temperature treatment and quench (*HQ*), the
 144 measured composition (SEM EDS) is uniformly $\text{Ti}_{0.98(1)}\text{Ni}_{1.13(1)}\text{Sn}_{1.00(1)}$, indicating the presence of
 145 excess Ni in the half-Heusler. The contrast in this image arises due to grain orientation. While XRD
 146 indicated the presence of some Heusler phase in sample *HQ*, only one phase is identified by SEM
 147 [Figure 5(b)] or TEM [Figure 6(b)], which is homogeneous displaying only bend contours. Upon low

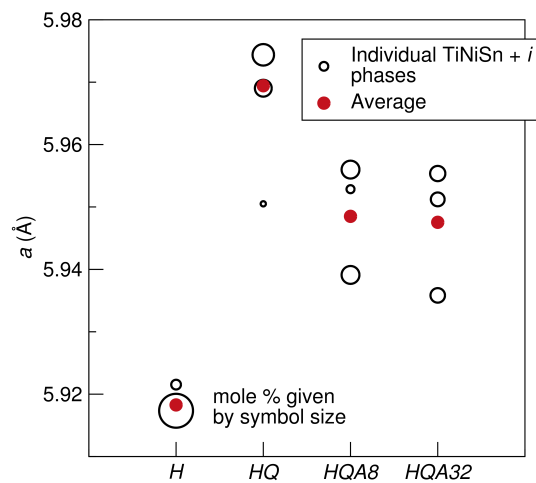


Figure 4. Lattice parameters for each of the half-Heusler phases fit using Rietveld refinement. Symbol size of the open circles corresponds to the mole percent of each contribution. The weighted average lattice parameter of the half-Heusler phases in each sample is given by the red filled circles, and is maximized for the *HQ* sample where the most Ni interstitials are trapped in the half-Heusler structure. Annealed samples have a large range of lattice parameters, and the distribution has shifted to a lower lattice parameter than the *HQ* sample.

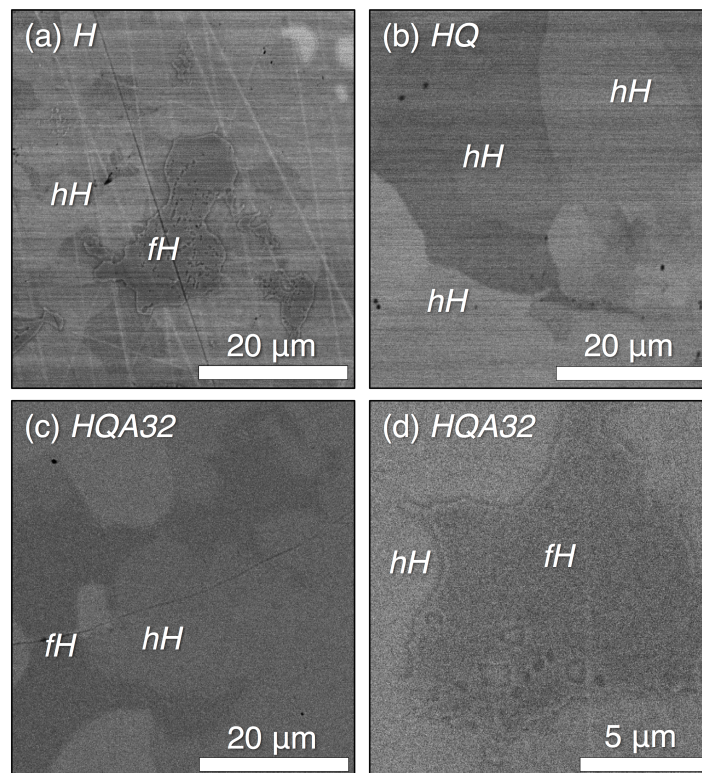


Figure 5. BSE SEM micrographs show orientation and phase contrast in samples (a) *H*, (b) *HQ*, and (c),(d) *HQA32*, enabling analysis of microstructure evolution. (a) The homogenized sample contains separate TiNiSn and TiNi₂Sn regions. (b) After quenching from high temperature, we do not observe the Heusler phase, but homogeneous half-Heusler that, according to EDS, contains excess Ni. In (c), low temperature annealing reintroduces the Heusler phase, as detailed in (d).

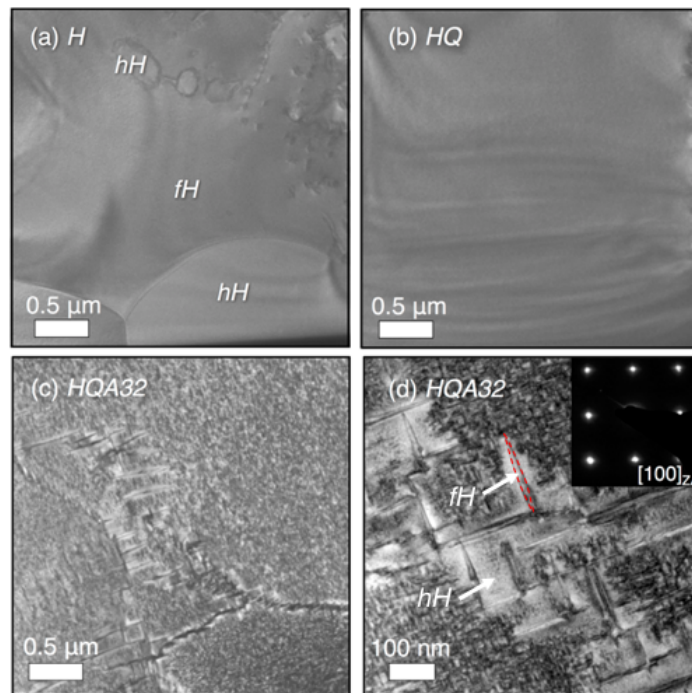


Figure 6. Transmission electron micrographs showing microstructural evolution in samples (a) *H*, (b) *HQ*, and (c),(d) *HQA32*. (a) The homogenized sample contains separate TiNiSn and TiNi_2Sn regions on the micron scale. (b) Quenching from high temperature again reveals a single phase with excess Ni. (c), (d) Bright field images (along the $[100]$ zone axis, shown by the inset in (d)) of *HQA32* show the Heusler phase precipitates out on the nanoscale, forming along $\langle 100 \rangle$ directions of the half-Heusler matrix, with larger precipitates forming along low angle grain boundaries. One of these larger precipitates is outlined in red. The mottled texture of (c) and (d) is due to smaller scale precipitates.

148 temperature annealing *HQA32*, we again identify the Heusler phase, as highlighted in 5(c) and (d).
 149 These large scale Heusler precipitates likely formed during the initial solidification, and never underwent
 150 complete dissolution into the half-Heusler matrix during the high temperature heat treatment. TEM is
 151 used to elucidate the reformation of the Heusler from the supersaturated $\text{TiNi}_{1.1}\text{Sn}$ phase.

152 Low temperature annealing of the homogeneous $\text{TiNi}_{1.1}\text{Sn}$ phase forms nanoscale Heusler
 153 precipitates with a high aspect ratio, shown in Figure 6(c). This microstructure has been observed
 154 by Verma *et al.* [28] These precipitates are semicoherent with the half-Heusler matrix, forming with a
 155 cube-on-cube orientation relationship along the $\langle 100 \rangle$ directions of the half-Heusler. Larger precipitates
 156 form along low angle grain boundaries, likely due to increased diffusion of Ni along the grain boundary.
 157 This could also be to accommodate strain at the grain boundary. The light regions around these larger
 158 precipitates are depleted of excess Ni, and so we do not see smaller precipitates in these regions. Heusler
 159 precipitates in the bulk of the half-Heusler grains are < 50 nm. The nanostructuring as a result of these
 160 heat treatments leads to enhanced thermoelectric properties compared to the homogenized sample due
 161 to phonon scattering from a second phase on multiple length scales.

162 Physical properties

163 The room temperature physical properties for each sample are presented in Figure 7. The high
 164 temperature quenched sample, *HQ*, displays an enhanced Seebeck coefficient (a) and power factor (c),
 165 as well as a decrease in thermal conductivity (d). This leads to an overall increase in the thermoelectric
 166 figure of merit (e), zT . The enhancement of these properties decreases with annealing, or decreasing Ni
 167 interstitial abundance, as indicated by the trend line.

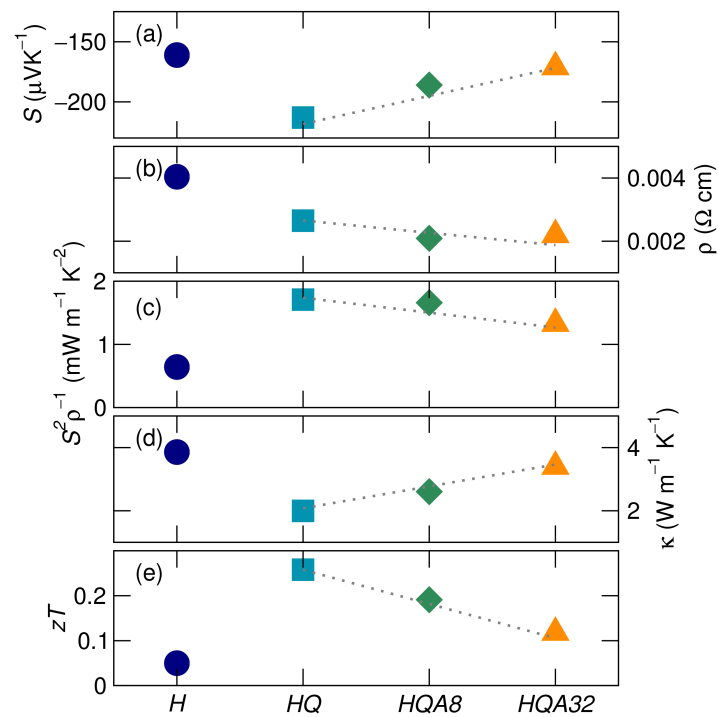


Figure 7. Thermoelectric physical properties for heat-treated samples with treatment identified on the x -axis. (a) The Seebeck coefficient is greatly enhanced for sample *HQ* and reduces with subsequent low temperature annealing. (b) Resistivity subtly decreases for *HQ* and limited change with annealing observed. As the (c) powerfactor is enhanced while (d) thermal conductivity is reduced, *HQ* has an improved figure of merit, (e) zT that is reduced with low temperature annealing, as shown in samples *HQA8* and *HQA32*. Dashed lines are guides to the eye.

168 Ni-interstitials act as electron donors, decreasing the electrical resistivity of samples after the high
 169 temperature quench [Figure 7(b)]. The increase in carrier concentration may be closer to optimal for
 170 these compounds, leading to a positive effect on the Seebeck coefficient.[34] The Seebeck coefficient
 171 increases in magnitude after the high temperature quench, and is maximized where the amount
 172 of Ni-interstitials is maximized [Figure 7(a)]. Calculations indicate that Ni-interstitials, or antisite
 173 defects where Ni sits on the interstitial site, cause “in-gap states,” leading to an experimental band
 174 gap of 0.12 eV, which is much smaller than the calculated band gap of 0.45 eV.[27,35,42,43] The Ni
 175 interstitials modify the density of states at the Fermi level, improving the Seebeck coefficient.[32,44–46]
 176 This interpretation follows the results presented earlier in the structural and microstructure sections of
 177 this contribution, as they describe an increase in Ni-interstitials for the quenched sample, and a decrease
 178 upon subsequent annealing. The phase separation present in the annealed samples could have a carrier
 179 filtering effect, selectively scattering low energy carriers due to the interfacial potential between the full
 180 and half-Heusler phases.[45]

181 The electrical properties of these samples are summarized by the thermoelectric power factor in
 182 Figure 7(c). Due to its enhanced Seebeck coefficient, the high temperature quenched sample (*HQ*) has
 183 the largest power factor. While subsequent annealing decreases the power factor back towards that of
 184 the homogenized sample, the decrease in electrical resistivity due to these heat treatments leads to an
 185 overall enhancement of the power factor compared to the homogenized sample.

186 Nickel interstitials also have a strong role in determining thermal conductivity, shown in Figure 7(d).
 187 As Ni-interstitials are introduced, they act as point defect phonon scattering centers, decreasing the
 188 lattice contribution to thermal conductivity.[3] The introduction of Ni interstitials due to the high
 189 temperature heat treatment and quench reduced thermal conductivity by almost a factor of two,
 190 from $3.86 \text{ W m}^{-1} \text{ K}^{-1}$ to $2.00 \text{ W m}^{-1} \text{ K}^{-1}$. While these measurements were conducted at 300 K, the
 191 contribution from point defects should increase with temperature due to the shortening mean free path
 192 of phonons. Low temperature annealing decreases the abundance of Ni-interstitials, and the thermal
 193 conductivity increases. However, the microstructure, which consisted of micron-scale precipitates in
 194 the homogenized sample, becomes nanostructured due to phase separation after the high temperature
 195 quench and low temperature anneal. This may lead to a permanent decrease in the overall thermal
 196 conductivity, as compared to the homogenized sample. There is ample evidence in the literature for
 197 increases in zT due to nano- and micro-scale phase separation in half-Heuslers.[11,22]

198 The zT of these materials has been calculated, as shown in Figure 7(e). Due to the impact of
 199 Ni-interstitials on both the Seebeck coefficient and the thermal conductivity, the quenched sample (*HQ*)
 200 has the largest room temperature $zT = 0.26$, over five times greater than zT of the homogenized sample
 201 ($zT = 0.05$). Further annealing of these samples decreases the quantity of Ni-interstitials, but leads
 202 to nanoscale Heusler precipitates within the half-Heusler matrix, giving a twofold increase in room
 203 temperature zT after 32 hours of low temperature annealing compared to homogenized $\text{TiNi}_{1.1}\text{Sn}$.

204 4. Conclusions

205 In this contribution, samples of $\text{TiNi}_{1.1}\text{Sn}$ were heat treated to determine the effect of Ni interstitials
 206 on physical properties. All samples were first homogenized in the biphasic regime, phase separating
 207 the full and half-Heusler. Next, samples were quenched from high temperature in the solid solution
 208 regime between TiNiSn and TiNi_2Sn , and final samples were annealed at low temperature for different
 209 time scales. The effect of processing on the prevalence of Ni interstitials was determined using
 210 synchrotron XRD and EDS, showing that when quenched from the solid solution regime, excess Ni
 211 was present in the half-Heusler TiNiSn tetrahedral vacancies. These observations were related to
 212 thermoelectric physical properties, showing that the Ni-interstitials enhance the Seebeck coefficient,
 213 while simultaneously reducing thermal conductivity, resulting in an improved zT by at least a factor
 214 of five. Subsequent annealing reduces the Ni-interstitials and reforms TiNi_2Sn on the nanoscale,
 215 which displays enhanced thermoelectric properties compared to the homogenized sample due to
 216 nanostructuring. While Ni interstitials in $\text{TiNi}_{1.1}\text{Sn}$ would be annealed out over time at the operating

temperature of this thermoelectric, this study showed the disorder from interstitial point defects have a positive effect on the thermal conductivity and Seebeck coefficient, and result in significantly higher figures of merit. In addition, the heat treatment process to form a solid solution and re-precipitate out the Heusler phase provides a route to nanostructuring of the bulk half-Heusler with excess Ni, and increasing the figure of merit with respect to homogenized $\text{TiNi}_{1.1}\text{Sn}$.

Acknowledgments: The research reported here was supported by the Materials Research Science and Engineering Center at UCSB: MRSEC NSF DMR 1720256 through IRG-1. M.L.C.B. is supported by the National Science Foundation Graduate Research Fellowship Program under Grant No. 1144085. Use of the Advanced Photon Source at Argonne National Laboratory was supported by the U. S. Department of Energy, Office of Science, Office of Basic Energy Sciences, under Contract No. DE-AC02-06CH11357.

Conflicts of Interest: The authors declare no conflict of interest. The funding sponsors had no role in the design of the study; in the collection, analyses, or interpretation of data; in the writing of the manuscript, and in the decision to publish the results.

Author Contributions: Conceptualization, Tresa Pollock; Funding acquisition, Tresa Pollock and Ram Seshadri; Investigation, Emily Levin, Francesca Long, Jason Douglas, Malinda Buffon and Leo Lammontagne; Project administration, Tresa Pollock and Ram Seshadri; Supervision, Tresa Pollock and Ram Seshadri; Visualization, Emily Levin; Writing, original draft, Emily Levin; Writing, review & editing, Tresa Pollock and Ram Seshadri.

References

- Snyder, G.J.; Toberer, E.S. Complex thermoelectric materials. *Nat. Mater.* **2008**, *7*, 105–114.
- Smith, K.; Thornton, M. Feasibility of thermoelectrics for waste heat recovery in conventional vehicles. *U.S. Department of Energy* **2009**.
- Biswas, K.; He, J.; Blum, I.D.; Wu, C.; Hogan, T.P.; Seidman, D.N.; Draid, V.; Kanatzidis, M.G. High-performance bulk thermoelectrics with all-scale hierarchical architectures. *Nature* **2012**, *489*, 414–418.
- Zeier, W.G.; Zevalkink, A.; Gibbs, Z.M.; Hautier, G.; Kanatzidis, M.G.; Snyder, G.J. Thinking like a chemist: Intuition in thermoelectric materials. *Angew. Chem. Int. Ed.* **2016**, *55*, 6826–6841.
- Lkhagvasuren, E.; Fu, C.; Fecher, G.H.; Auffermann, G.; Kreiner, G.; Schnelle, W.; Felser, C. Improved thermoelectric properties of TiNiSn through enhancing strain field fluctuation. *J. Phys. D: Appl. Phys.* **2017**, *50*, 425502.
- Bos, J.W.G.; Downie, R.A. Half-Heusler thermoelectrics: a complex class of materials. *J. Phys.: Condens. Matter* **2014**, *26*, 433201.
- Shen, Q.; Chen, L.; Goto, T.; Hirai, T.; Yang, J.; Meisner, G.P.; Uher, C. Effects of partial substitution of Ni by Pd on the thermoelectric properties of ZrNiSn-based half-Heusler compounds. *Appl. Phys. Lett.* **2001**, *79*, 4165–4167.
- Culp, S.R.; Poon, S.J.; Hickman, N.; Tritt, T.M.; Blumm, J. Effect of substitutions on the thermoelectric figure of merit of half-Heusler phases at 800°C. *Appl. Phys. Lett.* **2006**, *88*, 042106.
- Bhattacharya, S.; Pope, A.L.; Littleton, R.T.; Tritt, T.M.; Ponnambalam, V.; Xia, Y.; Poon, S.J. Effect of Sb doping on the thermoelectric properties of Ti-based half-Heusler compounds, $\text{TiNiSn}_{1-x}\text{Sb}_x$. *Appl. Phys. Lett.* **2000**, *77*, 2476.
- Fu, C.; Wu, H.; Liu, Y.; He, J.; Zhao, X.; Zhu, T. Enhancing the figure of merit of heavy-band thermoelectric materials through hierarchical phonon scattering. *Adv. Sci.* **2016**, *3*, 1600035.
- Downie, R.A.; MacLaren, D.A.; Bos, J.W.G. Thermoelectric performance of multiphase XNiSn (X = Ti, Zr, Hf) half-Heusler alloys. *J. Mater. Chem. A* **2014**, *2*, 6107.
- Bhattacharya, S.; Tritt, T.M.; Xia, Y.; Ponnambalam, V.; Poon, S.J.; Thadhani, N. Grain structure effects on the lattice thermal conductivity of Ti-based half-Heusler alloys. *Appl. Phys. Lett.* **2002**, *81*, 43–45.
- Joshi, G.; Yan, X.; Wang, H.; Liu, W.; Chen, G.; Ren, Z. Enhancement in thermoelectric figure-of-merit of an N-type half-Heusler compound by the nanocomposite approach. *Adv. Energy Mater.* **2011**, *1*, 643–647.
- Birkel, C.S.; Douglas, J.E.; Lettiere, B.R.; Seward, G.; Verma, N.; Zhang, Y.; Pollock, T.M.; Seshadri, R.; Stucky, G. Improving the thermoelectric properties of half-Heusler TiNiSn through inclusion of a second full-Heusler phase: microwave preparation and spark plasma sintering of $\text{TiNi}_{1+x}\text{Sn}$. *Phys. Chem. Chem. Phys.* **2013**, *15*, 6990.

- 269 15. Douglas, J.E.; Birkel, C.S.; Verma, N.; Miller, V.M.; Miao, M.S.; Stucky, G.D.; Pollock, T.M.; Seshadri, R.
270 Phase stability and property evolution of biphasic Ti-Ni-Sn alloys for use in thermoelectric applications. *J.*
271 *Appl. Phys.* **2014**, *115*, 043720.
- 272 16. Buffon, M.L.C.; Laurita, G.; Verma, N.; Lamontagne, L.; Ghadbeigi, L.; Lloyd, D.L.; Sparks, T.D.; Pollock,
273 T.M.; Seshadri, R. Enhancement of thermoelectric properties in the Nb-Co-Sn half-Heusler/Heusler system
274 through spontaneous inclusion of a coherent second phase. *J. Appl. Phys.* **2016**, *120*, 075104.
- 275 17. Lkhagvasuren, E.; Ouardi, S.; Fecher, G.H.; Auffermann, G.; Kreiner, G.; Schnelle, W.; Felser, C. Optimized
276 thermoelectric performance of the n-type half-Heusler material TiNiSn by substitution and addition of Mn.
277 *AIP Adv.* **2017**, *7*, 045010.
- 278 18. Populoh, S.; Aguirre, M.H.; Brunko, O.C.; Galazka, G.; Lu, Y.; Weidenkaff, A. High figure of merit in
279 (Ti,Zr,Hf)NiSn half-Heusler alloys. *Scr. Mater.* **2012**, *66*, 1073–1076.
- 280 19. Rausch, E.; Balke, B.; Ouardi, S.; Felser, C. Enhanced thermoelectric performance in the p-type half-Heusler
281 (Ti/Zr/Hf)CoSn_{0.8}Sn_{0.2} system via phase separation. *Phys. Chem. Chem. Phys.* **2014**, *16*, 25258.
- 282 20. Page, A.; Van der Ven, A.; Poudeu, P.F.P.; Uher, C. Origins of phase separation in thermoelectric
283 (Ti,Zr,Hf)NiSn half-Heusler alloys from first principles. *J. Mater. Chem.* **2016**, *4*, 13949.
- 284 21. Downie, R.A.; Popuri, S.R.; Ning, H.; Reece, M.J.; Bos, J.W.G. Effect of spark plasma sintering on the
285 structure and properties of Ti_{1-x}Zr_xNiSn half-Heusler alloys. *Materials* **2014**, *7*, 7093–7104.
- 286 22. Downie, R.A.; Barczak, S.A.; Smith, R.I.; Bos, J.W.G. Compositions and thermoelectric properties of XNiSn
287 (X = Ti, Zr, Hf) half-Heusler alloys. *J. Mater. Chem. C* **2015**, *3*, 10534.
- 288 23. Yamashita, O.; Tomiyoshi, S.; Makita, K. Bismuth telluride compounds with high thermoelectric figures of
289 merit. *J. Appl. Phys.* **2003**, *93*, 368–374.
- 290 24. Goldsmid, H.J. Thermoelectric refrigeration. (*Plenum, New York, 1964*).
- 291 25. Poudel, B.; Hao, Q.; Ma, Y.; Lan, Y.; Minnich, A.; Yu, B.; Yan, X.; Wang, D.; Muto, A.; Vashaee, D.; Chen, X.;
292 Liu, J.; Dresselhaus, M.S.; Chen, G.; Ren, Z. High-thermoelectric performance of nanostructured bismuth
293 antimony telluride bulk alloys. *Science* **2008**, *320*, 634–638.
- 294 26. Hsu, K.F.; Loo, S.; Guo, F.; Chen, W.; Dyck, J.S.; Uher, C.; Hogan, T.; Polychroniadis, E.K.; Kanatzidis, M.G.
295 Cubic AgPb_mSbTe_{2+m}: Bulk thermoelectric materials with high figure of merit. *Science* **2004**, *303*, 818–821.
- 296 27. Douglas, J.E.; Chater, P.A.; Brown, C.M.; Pollock, T.M.; Seshadri, R. Nanoscale structural heterogeneity in
297 Ni-rich half-Heusler TiNiSn. *J. Appl. Phys.* **2014**, *116*, 163514.
- 298 28. Verma, N.; Douglas, J.E.; Kramer, S.; Pollock, T.M.; Seshadri, R.; Levi, C.G. Microstructure Evolution of
299 Biphasic TiNi_{1+x}Sn Thermoelectric Materials. *Mat. Trans. A* **2016**, *47*, 4116.
- 300 29. Levin, E.E.; Bocarsly, J.D.; Wyckoff, K.E.; Pollock, T.M.; Seshadri, R. Tuning the magnetocaloric response in
301 half-Heusler/Heusler MnNi_{1+x}Sb solid solutions. *Phys. Rev. Mater.* **2017**, *1*, 075003(1–8).
- 302 30. Downie, R.A.; MacLaren, D.A.; Smith, R.I.; Bos, J.W.G. Enhanced thermoelectric performance in
303 TiNiSn-based half-Heuslers. *Chem. Commun.* **2013**, *49*, 4184.
- 304 31. Denton, A.; Ashcroft, N. Vegard's law. *Phys. Rev. A* **1991**, *43*, 3161.
- 305 32. Hazama, H.; Matsubara, M.; Asahi, R.; Takeuchi, T. Improvement of thermoelectric properties for
306 half-Heusler TiNiSn by interstitial Ni defects. *J. Appl. Phys.* **2011**, *110*, 063710.
- 307 33. Barczak, S.A.; Buckman, J.; Smith, R.I.; Baker, A.R.; Don, E.; Forbes, I.; Bos, J.W.G. Impact of interstitials
308 Ni on the thermoelectric properties of the half-Heusler TiNiSn. *Materials* **2018**, *11*, 536.
- 309 34. Xie, H.; Wang, H.; Fu, C.; Liu, Y.; Snyder, G.J.; Zhao, X.; Zhu, T. The intrinsic disorder related alloy
310 scattering in ZrNiSn half-Heusler thermoelectric materials. *Scientific Reports* **2014**, *4*, 6888.
- 311 35. Miyamoto, K.; Kimura, A.; Sakamoto, K.; Ye, M.; Cui, Y.; Shimada, K.; Namatame, H.; Taniguchi, M.;
312 Fujimori, S.; Saitoh, Y.; Ikenaga, E.; Kobayashi, K.; Tadano, J.; Kanomata, T. In-gap electronic states
313 responsible for the excellent thermoelectric properties of Ni-based half-Heusler alloys. *Applied Physics*
314 *Express* **2008**, *1*, 081901.
- 315 36. Mott, N.F.; Jones, H. The theory of the properties of metals. *Clarendon Press, Oxford* **1936**.
- 316 37. Coelho, A. Topas Academic V5 Software. <http://www.topas-academic.net/>, 2012.
- 317 38. Momma, K.; Izumi, F. VESTA 3 for three-dimensional visualization of crystal, volumetric and morphology
318 data. *J. Appl. Cryst.* **2011**, *44*, 1272–1276.
- 319 39. Graf, T.; Felser, C.; Parkin, S. Simple rules for the understanding of Heusler compounds. *Prog. Solid State*
320 *Chem.* **2011**, *39*, 1–50.

- 321 40. Kandpal, H.C.; Felser, C.; Seshadri, R. Covalent bonding and the nature of band gaps in some half-Heusler
322 compounds. *J. Phys. D: Appl. Phys.* **2006**, *39*, 776–785.
- 323 41. Lloyd, G.E. Atomic number and crystallographic contrast images with the SEM: a review of backscattered
324 electron techniques. *Mineral. Mag.* **1987**, *51*, 3–19.
- 325 42. Aliev, F.G. Gap at Fermi level in some new d- and f-electron intermetallic compounds. *Physica B* **1991**,
326 *171*, 199.
- 327 43. Larson, P.; Mhanti, S.D.; Kanatzidis, M.G. Structural stability of Ni-containing half-Heusler compounds.
328 *Phys. Rev. B* **2000**, *62*, 12754.
- 329 44. Colinet, C.; Jund, P.; Tedenac, J.C. NiTiSn a material of technological interest: Ab initio calculations of
330 phase stability and defects. *Intermetallics* **2014**, *46*, 103.
- 331 45. Zhang, Y.; Bahk, J.; Lee, J.; Birkel, C.S.; Snedaker, M.L.; Liu, D.; Zeng, H.; Moskovits, M.; Shakouri,
332 A.; Stucky, G.D. Hot carrier filtering in solution processed heterostructures: a paradigm for improving
333 thermoelectric efficiency. *Adv. Mater.* **2014**, *26*, 2755–2761.
- 334 46. Heremans, J.P.; Jovovic, V.; Toberer, E.S.; Saramat, A.; Kurosaki, K.; Charoenphakdee, A.; Yamanaka, S.;
335 Snyder, G.J. Enhancement of thermoelectric efficiency in PbTe by distortion of the electronic density of
336 states. *Science* **2008**, *321*, 554–557.